International Communications in Heat and Mass Transfer 134 (2022) 106048

Contents lists available at ScienceDirect

International Communications in Heat and Mass Transfer

journal homepage: www.elsevier.com/locate/ichmt

# Transport and wall surface deposition of airborne particles in enclosed, buoyancy-driven turbulent flows using fully-resolved numerical simulations

Alexandre Fabregat [a,*], Jordi Pallarès [a]

[a] Deparment of Mechanical Engineering, Universitat Rovira i Virgili, Av. Països Catalans, 26, 43007 Tarragona, Spain

ARTICLE INFO

*Keywords:*
Natural convection
Turbulent transport
Direct numerical simulation
Wall particle deposition
Thermophoresis
Brownian motion

ABSTRACT

Airborne particle transport and deposition on solid surfaces play a key role in aerosol deposition, infectious diseases transmission and surface soiling. Moving fluids disperse particles by the action of several forces including drag, lift, thermophoresis, buoyancy and Brownian effects. The relative importance of each contribution depends on the phases density ratio and the particle size. These two parameters, along with the characteristics of the boundary layers, control the local wall deposition rate. Experiments and analytical solutions have provided partial information on deposition velocity for several particle sizes and turbulent intensities in air filled cavities. While experimental data is restricted to few selected wall locations, boundary layer models results only provide wall-average values. Using Direct Numerical Simulations to solve the flow hydrodynamics and Exponential-Lagrangian Tracking Schemes for the disperse phase, deposition rates on each surface of a cubical cavity with oppositely heated walls have been determined. Numerical results at $Ra = 5.4 \times 10^8$ are in very good agreement with experiments for 0.1 and 0.5 μm particle diameters. Deposition rate on adiabatic walls is found to be spatially inhomogeneous with particles accumulating near the corners where hot and cold walls meet. These preferential spots are explained by intensified wall-normal turbulent transport in these particular regions.

## 1. Introduction

Understanding the transport and deposition of dispersed phases in the form of particles, droplets or aerosols by the action of a moving fluid is key in a wide range of processes of technological, biological and industrial interest. Applications range from indoor air quality [1], dispersion of airborne virus-laden droplets produced when talking, coughing or sneezing capable of spreading infectious diseases [2,3], obstruction of flow due to accumulation of particulate biological material on the inner walls of blood vessels [4] or soiling of valuable surfaces due to dust deposition [5].

The determination of the particle deposition rate on thermally active surfaces has been the subject of both experimental and numerical efforts [6–10]. The specific case for flows in rectangular cavities with differentially heated walls has attracted a considerable amount of attention [11–19]. Of particular interest is the work of Thatcher et al. [20] who used a cubical cavity of 1.22 m filled with air to determine the accumulation rate of particles for two different Rayleigh numbers. The flow was driven by imposing a constant temperature $T_c$ on the bottom and one vertical wall while keeping the opposite walls at $T_c = T_h - 3$ K ($Ra = 5.4 \times 10^8$) and $T_c = T_h - 10$ K ($Ra = 3.6 \times 10^9$). The other two vertical opposed walls were thermally insulated. This specific configuration generates a buoyancy-driven dominant recirculation where the fluid moves upward along the vertical hot wall and downward along the cold one. After seeding particles of different sizes ranging from 0.1 to 2.5 μm, the dispersed phase was allowed to circulate for several turnover times to ensure statistically converged conditions. The deposition rate for each case was determined by counting the number of deposited particles on several sampling areas distributed along the main cavity bisector. The results provided data at seven discrete positions regularly distributed on each four thermally active walls.

The hydrodynamics of the $Ra = 5.4 \times 10^8$ case reported by Thatcher et al. [20] was numerically reproduced by Fabregat and Pallarès [21] who used Direct Numerical Simulations (DNS) to solve the momentum and heat transport equations. After characterizing the momentum and thermal boundary layers using time-averaged profiles of velocity and temperature, Pallarès and Fabregat [22] derived mixed boundary layer models for each thermally active wall. The resulting self-similar solution

* Corresponding author.
*E-mail addresses:* alexandre.fabregat@urv.cat (A. Fabregat), jordi.pallares@urv.cat (J. Pallarès).

https://doi.org/10.1016/j.icheatmasstransfer.2022.106048

Available online 22 April 2022

was used to advect a scalar representing particle concentration. Estimates of the wall-average deposition rates were found to agree well with the experimental results of Thatcher et al. [20] for 0.1 μm (thermophoresis dominated regime) and 0.5 μm (buoyancy dominated regime).

Both experiments and numerical studies provided partial information on particle deposition either by reporting rates at selected positions in the case of Thatcher et al. [20] or by idealizing the boundary layer flow to be homogeneous, two-dimensional and stationary. To gain insight on the local transport of the dispersed phase across the entire cavity surface extension, here a DNS of the turbulent hydrodynamics is coupled with a particle transport model accounting for drag and lift, thermophoresis, buoyancy and Brownian forces [23]. The relative importance of each force term depends on the particle size, the ratio of densities between the phases and the local flow characteristics. The detailed maps of particle deposition for each wall allows to identify significant spatial inhomogeneities in accumulation rates and identify preferential deposition spots missed in both previous experimental and analytical studies.

## 2. Mathematical model and numerics

A sketch of the computational domain consisting in a cubical cavity filled with air with coordinate origin located at the center is shown in Fig. 1(a). Following the flow set-up used by Thatcher et al. [20], the cavity, with a wall side length of $l_s = 1.22$m, is heated by imposing a constant temperature $T_h = 301.5$K at the bottom and left walls, i.e. $\widetilde{T}(\widetilde{x}, -l_s/2, \widetilde{z}) = \widetilde{T}(-l_s/2, \widetilde{y}, \widetilde{z}) = T_h$ (depicted in red), and cooled by imposing a constant temperature $T_c = 298.5$K at the top and right, $\widetilde{T}(\widetilde{x}, l_s/2, \widetilde{z}) = \widetilde{T}(l_s/2, \widetilde{y}, \widetilde{z}) = T_c$ (in blue). Front and back walls are considered adiabatic (note the use of a tilde to denote dimensional variables).

All physical properties for both phases are evaluated at the reference temperature $T_0 = (T_h + T_c)/2 = 300$K and assumed constant. The continuous phase (air) density, thermal diffusion kinematic viscosity, thermal expansion coefficient and thermal conductivity are $\rho_0 = 1.3$ kg m$^{-3}$, $\alpha = 2.24 \times 10^{-5}$m$^2$s$^{-1}$, $\nu = 1.57 \times 10^{-5}$m$^2$s$^{-1}$, $\beta = 1/300$K$^{-1}$ and $k_f = 0.026$Wm$^{-1}$K$^{-1}$, respectively. The dispersed phase (particles) density and thermal conductivity are $\rho_p = 1350.0$kgm$^{-3}$ and $k_p = 0.430$Wm$^{-1}$K$^{-1}$ respectively.

The main flow feature for the thermal configuration shown in Fig. 1

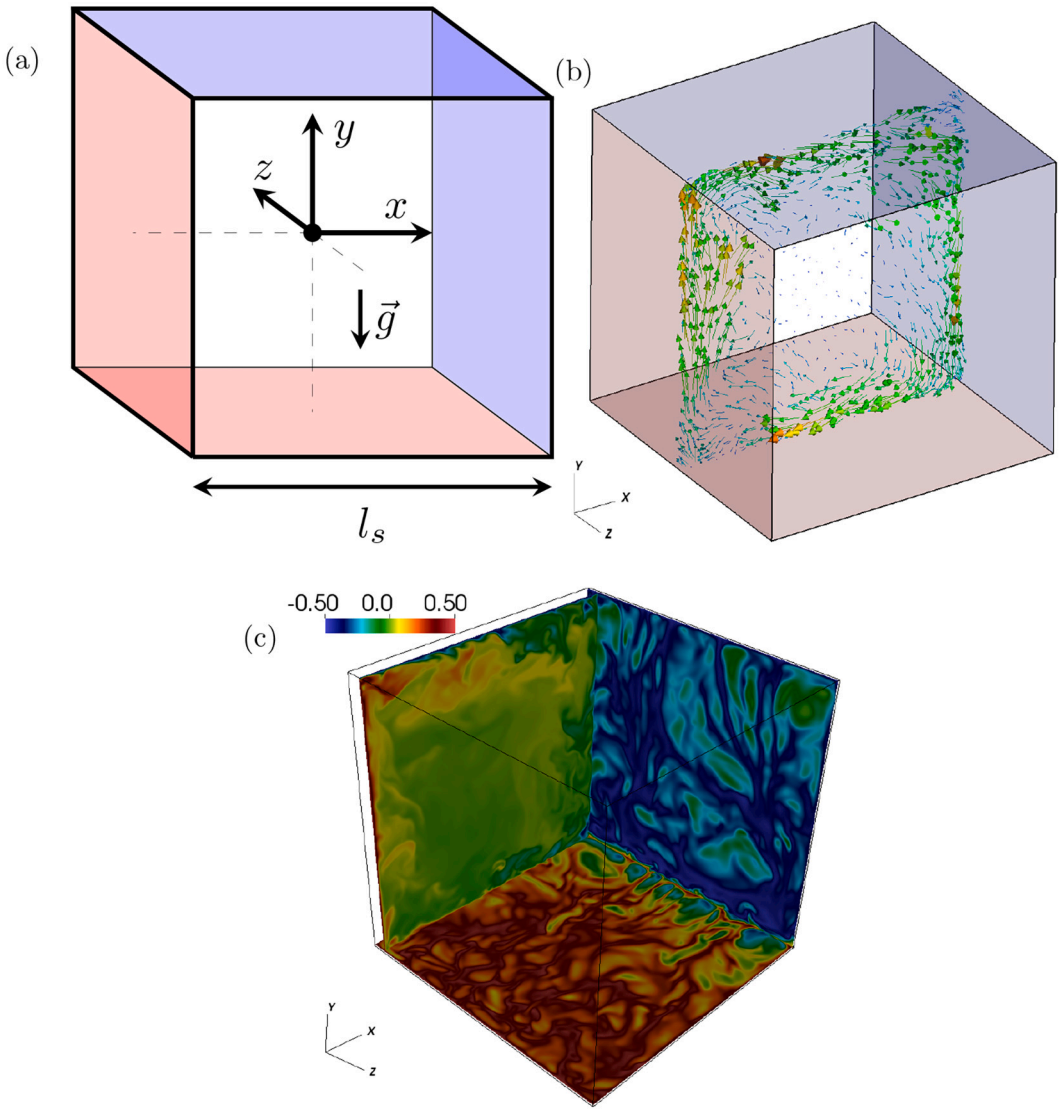


**Fig. 1.** Panel (a): Domain sketch showing the coordinate system. Hot and cold in red and blue respectively. Panel (b): Slice at $z = 0$ of an instantaneous velocity field showing the dominant rotating flow feature. Panel (c): Near wall slices of an instantaneous temperature field in each coordinate direction. (For interpretation of the references to colour in this figure legend, the reader is referred to the web version of this article.)

(a) is a clockwise recirculation (as seen from $+z$) generated by the upward flow along the hot cold and downward along the cold one. An instantaneous snapshot of the developed turbulent velocity field at $z = 0$ showing this persistent large scale eddy is depicted in Fig. 1(b). To illustrate the turbulent flow features, Fig. 1(c) shows three slices in each coordinate direction of an instantaneous temperature fluctuation field defined as $\theta = (\widetilde{T} - T_0)/(T_h - T_c) = (\widetilde{T} - T_0)/T_s$.

### 2.1. Carrier phase: hydrodynamics

Assuming incompressibility conditions and Boussinesq approximation and neglecting radiation and viscous heating effects, the non-dimensional mass, momentum and heat conservation equations can be written as:

$$\frac{\partial u_i}{\partial x_i} = 0 \tag{1}$$

$$\frac{\partial u_i}{\partial t} + u_j\frac{\partial u_i}{\partial x_j} = -\frac{\partial p}{\partial x_i} + \frac{Pr}{\sqrt{Ra}}\frac{\partial^2 u_i}{\partial x_j \partial x_j} + Pr\theta\delta_{i2} \tag{2}$$

$$\frac{\partial \theta}{\partial t} + u_j\frac{\partial \theta}{\partial x_j} = \frac{1}{\sqrt{Ra}}\frac{\partial^2 \theta}{\partial x_j \partial x_j} \tag{3}$$

where $t$ is time, $u_i$ is the velocity component in the direction $x_i$, $p$ is pressure, $\delta_{ij}$ is the Kronecker delta and $Ra = (g\beta T_s l_s^3)/(\nu\alpha) = 5.4 \times 10^8$ and $Pr = \nu/\alpha = 0.7$ are the Rayleigh and Prandtl groups respectively. The length, velocity, time and temperature scales are $l_s = 1.22$m, $u_s = \alpha Ra^{1/2}/l_s$=0.427 ms$^{-1}$, $t_s = l_s/u_s$=2.86 s and $T_s = 3K$ respectively. Note that the equation of state that relates fluid density $\rho_f$ and temperature fluctuation $\theta$ under the Boussinesq approximation can be written as $\rho_f = \rho_0(1 - \beta(\widetilde{T} - T_0)) = \rho_0(1 - \beta T_s\theta)$.

Eqs. (1)–(3) are solved using the solver Nek5000 [24]. Explicit resolution of all spatial and temporal scales has been guaranteed by meeting the resolution criteria proposed by Scheel et al. for similar buoyancy driven flow configurations [25]. Details on numerics and mesh resolution for the hydrodynamics are provided in Fabregat and Pallarès [21].

### 2.2. Dispersed phase: particle transport

Assuming spherical and smooth particles, the position of a given particle $x_i$* is given by:

$$\frac{dx_i^*}{dt} = u_i^* \tag{4}$$

where the particle velocity $u_i$* can be determined by solving the force balance on the particle expressed as:

$$\frac{du_i^*}{dt} = \underbrace{\frac{u_i - u_i^*}{\tau_p}}_{\text{Drag}} + \underbrace{n_g\delta_{i2}}_{\text{Buoyancy}} + \underbrace{n_{th}\frac{\partial T}{\partial x_i}}_{\text{Thermophoresis}} + \underbrace{n_l\varepsilon_{ijk}\left[u_j^* - u_j\right]\omega_k}_{\text{Lift}} + \underbrace{n_i(t)}_{\text{Brownian}} \tag{5}$$

where $\varepsilon$ is the Levi-Civita symbol and $\vec{\omega} = \nabla \times \vec{u}$ is the flow vorticity. The particle transport model presented in Eqs. (4)–(5) assumes that there are five relevant forces acting on the particle, namely, hydrodynamic drag and lift, buoyancy, thermophoresis and Brownian. Under the one-way coupling approach, the carrier phase directly affects the particle transport through drag, lift and thermophoresis. Contrarily, the dispersed phase is assumed to have negligible contributions to the carrier phase momentum conservation. This assumption is valid for small enough particles and dilute conditions as those used in the experiments carried out by Thatcher et al. [20]. In Eq. (5) the accelerations originated from the pressure gradient force, the added mass force and the Basset force are neglected. Lubrication forces associated to the pressure gradient generated when two solid surfaces approach each other have also been neglected due to the small values of normal-to-wall velocity component prior to deposition and the reduced local effective air viscosity expected due to non-continuum effects when the particle size is only one order of magnitude larger than the air mean free path [26,27]. Each contribution to the particle transport in Eq. (5) along with the definitions of quantities $\tau_p$, $n_g$, $n_{th}$, $n_l$ and $n_i$ are discussed next.

#### 2.2.1. Drag

Hydrodynamic drag accounts for the fluid resistance or friction a particle experiences as it moves with respect to the carrier phase. The hydrodynamic drag can be characterized by the particle Stokes number $\tau_p$ defined as the ratio of the particle and flow characteristic times. Small Stokes numbers are associated to particles that rapidly react to changes in accelerations in the underlying flow while large Stokes are found in inertia-dominated particles.

The non-dimensional Stokes number for a particle of diameter $d_p$ can be written as [28]:

$$\tau_p = \frac{d_p^2}{18C_c}\frac{\rho_p}{\mu_f}\frac{u_s}{l_s} \tag{6}$$

where $C_c$ is a correction factor that depends on the Knudsen number $Kn$ such that [29].

$$Kn = \frac{2\lambda}{d_p}, \qquad C_c = 1 + Kn\left[1.205e^{-0.0026/Kn} + 0.425e^{-0.7400/Kn}\right] \tag{7}$$

where $\lambda = 6.8 \times 10^{-8}$ m is the free mean path for air at $T_0$.

The estimated Stokes number for 0.1 and 0.5 μm are $8 \times 10^{-8}$ and $3 \times 10^{-9}$ respectively.

#### 2.2.2. Buoyancy (weight)

The magnitude of the buoyancy force experienced by a particle immersed in a fluid with different density under a gravitational field with acceleration magnitude $g = 9.8$ms$^{-2}$ can be written as:

$$n_g = -g\left(1 - \frac{\rho_f}{\rho_p}\right)\frac{l_s}{u_s^2}. \tag{8}$$

#### 2.2.3. Thermophoresis

Thermophoresis is the force due to gradients in the temperature field across the particle characteristic length, this is, $\widetilde{d}_p$ for a spherical particle. The pre-factor of the non-dimensional temperature gradient, $n_{th}$, is defined as:

$$n_{th} = -18\frac{K_{tp}}{d_p^2}\frac{\nu_f^2}{u_s^2}\frac{\rho_f}{\rho_p}\frac{T_s}{T_0} \tag{9}$$

where the factor $k_{tp}$, defined as [30],

$$K_{tp} = \frac{2C_s\left(k_f + 2k_pKn\right)\left[1 + 2Kn(1.2 + 0.41exp(-0.44/Kn))\right]}{(1 + 6C_mKn)\left(2k_f + k_p + 4k_pC_tKn\right)}, \tag{10}$$

contains three constant set to $C_s = 1.17$, $C_m = 1.14$ and $C_t = 2.18$. Note that the negative sign in $n_{th}$ indicates that the force points in the direction of maximal temperature decay.

#### 2.2.4. Lift

The hydrodynamic force acts perpendicular to the flow direction and is proportional to the cross product of the velocity difference between the two phases and the local vorticity in the carrier phase. The proportionality factor has the form

$$n_L = C_L\frac{\rho_f}{\rho_p} \tag{11}$$

where the lift coefficient $C_L$ is defined as [31].

$$C_L = \left[5.816\sqrt{\frac{Sr_p}{2Re_p}} - 0.875\frac{Sr_p}{2}\right]\frac{3}{4Sr_p}\frac{J(\varepsilon)}{2.255} \tag{12}$$

where the particle Reynolds number $Re_p$, $Sr_p$, $\varepsilon$ and $J$ are determined using the relations

$$Re_p = \left|u_i^* - u_i\right|\frac{dp}{l_s}Re, \qquad Sr_p = \frac{\left|\varepsilon_{ijk}\left[u_j^* - u_j\right]\omega_k\right|}{\left|u_j^* - u_j\right|^2}\frac{dp}{l_s}, \qquad \varepsilon = \sqrt{\frac{Sr_p}{Re_p}}, \tag{13}$$

$$J(\varepsilon) = 0.6765\{1 + tanh[2.5log_{10}(\varepsilon + 0.191)]\}\{0.677 + tanh[6(\varepsilon - 0.32)]\}. \tag{14}$$

#### 2.2.5. Brownian

For small enough particles, the net force due to molecular vibrations may not be negligible and, therefore, contribute to the transport. This Brownian force takes the form (see for example Ounis et al. [32]):

$$n_i(t) = Z_i(t)\sqrt{\frac{2\pi}{\Delta t}216\frac{\rho_f}{\rho_p^2}\frac{k_B T_0 \nu_f}{d_p^5 \pi^2 C_c}\frac{t_s^3}{l_s^2}} \tag{15}$$

where $k_B = 1.38064852 \times 10^{-23}$ JK$^{-1}$ is the Boltzmann constant and $Z_i(t)$ is a random number with a Gaussian distribution updated each time step of size $\Delta t$.

### 2.3. Exponential-Lagrangian tracking schemes

Classical explicit methods have been historically used to temporally integrate the transport equations of Lagrangian particles (fluid markers) with affordable computational costs. However, numerical integration of Eqs. (4)–(5) for relatively small values of $\tau_p$ is usually prohibitive due to numerical stability constrains. For example, 4-th order Runge-Kutta method requires time steps of the order $\Delta t < 2\tau_p$. To alleviate these stability requirements, Eqs. (4) and (5) are temporally integrated using Exponential-Lagrangian Tracking Schemes (ELTS) [33] which is inherently stable and offer, at least, a $\mathcal{O}(\Delta t^2)$ local truncation error.

## 3. Results

Particle deposition has been investigated by randomly seeding a total of $N = 10^6$ particles over the entire cavity volume once flow statistically steady conditions have been reached at $t \approx 150$. Such condition has been determined by analyzing the temporal convergence of instantaneous wall-averaged Nusselt numbers (see Fig. 3 in Fabregat et al. [21]). A particle is assumed to deposit when its distance from any wall is equal or smaller than its radius. In the event of deposition, the values of particle position, velocity, drag, thermophoresis, lift and Brownian forces are recorded (weight force value is constant for a given $d_p$) and the particle is randomly reseeded into the cavity keeping the total number of tracked particles constant (and equal to $N$). The $N$ particles have been transported for $\Delta t_d = 212$ (10.1 min) and $\Delta t_d = 93$ (4.4 min) time units for the 0.1 μm and 0.5 μm cases respectively. Over this time span, a total number of 1221 and 1799 particles have deposited for each particle size. The number of particles and deposition time span differ by several orders of magnitude from those in the experimental set-up by Thatcher et al. where two different experiments for each particle size used $N = 70$ and 32.5 billion particles over $\Delta\widetilde{t}_d = 141.1$ h and $\Delta\widetilde{t}_d = 88.2$ h for $d_p =$ 0.1 μm and $N = 103$ and 263 million particles over $\Delta\widetilde{t}_d = 94.4$ h and $\Delta\widetilde{t}_d = 93.3$ h for $d_p = 0.5$ μm. However, the deposition area considered in the experiments takes values between 0.4% and 10% of the total cavity surface where the exact value for each experiment could not be exactly determined.

Fig. 2 shows the spatial distribution of depositions obtained by plotting the impact locations on both horizontal walls (floor and ceiling on left and right panels respectively) for both particle diameters $d_p = 0.1$ μm (in black) and $d_p = 0.5$ μm (in red). The larger number of deposited particles on the ceiling suggests that small particle transport is dominated by thermophoresis. In contrast, large particles are dominated by buoyancy with most of the impacts registered on the cavity floor. Notably, while the large particles seem to homogeneously distribute over the entire horizontal wall, smaller particles tend to accumulate towards the left corner of the cavity, $x \lesssim -0.2$, where the vertical hot and the horizontal walls meet.

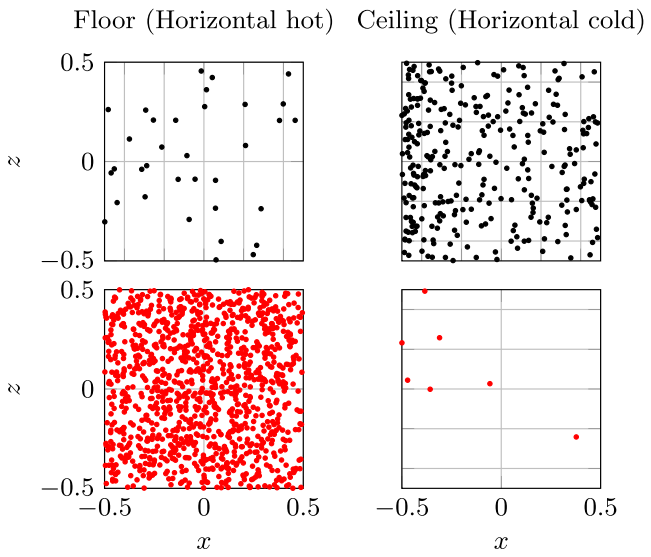


**Fig. 2.** Particle deposition locations for the horizontal hot (left) and cold (right) walls for two particles sizes: $\widetilde{d}_p = 0.1$ μm (black) and $\widetilde{d}_p = 0.5$ μm (red). (For interpretation of the references to colour in this figure legend, the reader is referred to the web version of this article.)

The relatively small number of $d_p = 0.1$ μm particles deposited on the floor or $d_p = 0.5$ μm particles deposited on the ceiling can be explained by the action of Brownian transport. The increasing contribution of the Brownian effects to the overall transport as particle size decreases explains the larger number of 0.1 μm particles deposited on the floor in

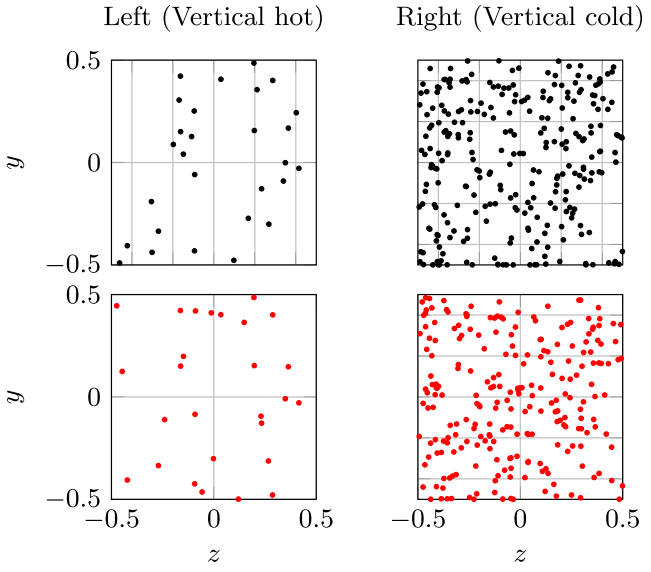


**Fig. 3.** Particle deposition locations for the vertical hot (left) and cold (right) walls for two particles sizes: $\widetilde{d}_p = 0.1$ μm (black) and $\widetilde{d}_p = 0.5$ μm (red). (For interpretation of the references to colour in this figure legend, the reader is referred to the web version of this article.)

comparison to the number of 0.5 μm particles on the ceiling.

Deposition on thermally active vertical walls is shown in Fig. 3. In the absence of gravity effects, thermophoresis dominates transport in the $y$ direction for both particles sizes and depositions concentrate on the cold wall. While no preferential distribution is found for large particles, small ones tend to accumulate in the vicinity of the corner where, again, the horizontal hot and vertical cold walls meet. Similarly, impacts on the hot vertical wall can be attributed to Brownian effects.

Deposition on the adiabatic walls is shown in Fig. 4. While inhomogeneities in the wall deposition velocity were modest on thermally active walls, adiabatic ones exhibit evident preferential spots in the areas where differently heated walls meet, this is, the top left (vertical hot meets horizontal cold) and bottom right (vertical cold meets horizontal hot) corners.

As shown in Fig. 5(a), intensification of wall-normal turbulent momentum flux $\langle w'^2 \rangle$ in the hot-cold corners near adiabatic surfaces (slice at $z = 0.499$ used here) can explain the inhomogeneous deposition rate on thermally passive walls shown in Fig. 4. Turbulent Reynolds stresses in the vertical $\langle v'w' \rangle$ and horizontal $\langle u'w' \rangle$ directions are shown in Fig. 5 (b) and (c) respectively. Results suggest that as fluid moves past the corner of deferentially heated walls, turbulent plumes grow parallel to the horizontal walls. This plume-like geometry elongating along the $x$ direction is also observed in the shape of the preferential deposition patches in Fig. 4.

The deposition velocity is defined as $v_d = M_s/(\Delta t_d \langle C \rangle A_d) = (N_d/N)(l_s/\Delta t_d)$ where $N_d$ is the number of deposited particles over the $\Delta t_d$ time span and $A_d$ area, $M_s = \rho_p A_d V_p$ is the total deposited mass, $V_p = (\pi/6)\tilde{d}_p^3$ is the particle volume and $\langle C \rangle = \rho_p N V_p / {l_s}^3$ is the bulk concentration of suspended particles. Numerical results on each thermally active wall are compared to experiments in Fig. 6. The experimental data, reported by Thatcher et al. [20], is comprised of two realizations (solid and empty markers) at seven locations per wall along the flow coordinate $s$. With origin at the bottom right corner, $s = 0$, this coordinate increases in the clockwise direction taking the values of $s = 1$, $s = 2$ and $s = 3$ at each corner, namely, bottom left, top left and top right respectively. Therefore, $s \equiv \frac{1}{2} - x$ for the horizontal hot wall (floor), $s \equiv y + \frac{3}{2}$ for the vertical hot wall, $s \equiv x + \frac{5}{2}$ for the horizontal cold wall (ceiling) and $s \equiv \frac{7}{2} - y$ for the vertical cold wall. It is important to note that these seven locations on each wall correspond to seven sampling extraction areas distributed along the main cavity bisector along $s$. (see Thatcher et al. [20] for details).

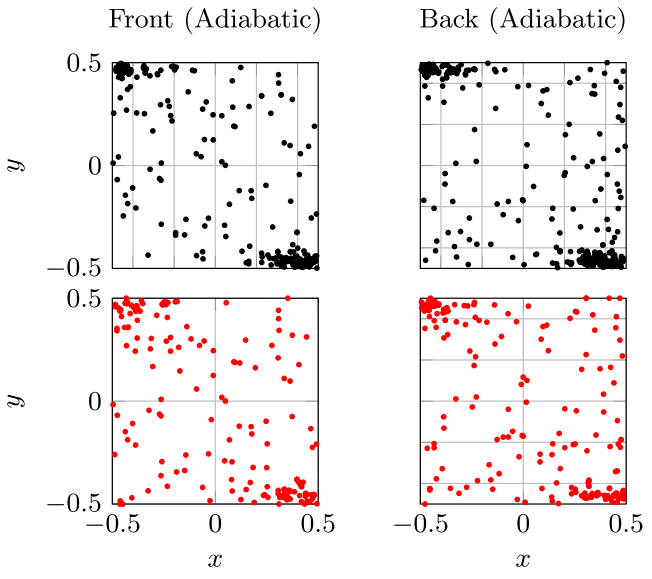


**Fig. 4.** Particle deposition locations for the two vertical adiabatic walls for two particles sizes: $\tilde{d}_p = 0.1$ μm (black) and $\tilde{d}_p = 0.5$ μm (red). (For interpretation of the references to colour in this figure legend, the reader is referred to the web version of this article.)

The numerical results shown in Fig. 6 as dashed blue lines correspond to wall-averaged deposition velocities over each entire wall. Despite the differences in the total number of particles, sampling area and time span and bulk concentration, numerical results are in good agreement with experiments for all four walls and two particle size associated to distinct deposition regimes. Predictions of the deposition velocity using laminar boundary layer models, reported by Pallares and Fabregat [22], are plotted in Fig. 6 with dotted lines. This model assumes that the flow within the boundary layers is steady and laminar and that the mass transfer for particles with small inertia is dominated by flow convection, thermophoresis and Brownian motion. Fig. 6 shows that, for the smallest particles, the boundary layer model estimates a more uniform deposition velocities for the different walls than the numerical simulations. For the particles of 0.5 μm, the relatively low flow unsteadiness within the boundary layers, captured by the numerical simulations but neglected in the boundary layer model, produces larger deposition velocities in the simulations than in the boundary layer approximation. For example, for the cold ceiling, the simulation predicts similar deposition velocities to the experiments while the boundary layer model estimates a zero deposition velocity at this wall because the downward settling velocity overcomes the thermophoretic and Brownian effects. Overall, it can be seen that both the numerical simulation and the boundary layer model reproduce the general trend reported in the experiments by Thatcher et al. [20].

Total deposition rate for the two particle sizes is shown in Fig. 7 as solid lines. For each case, dashed lines indicate the values that would result from deposition at the settling velocity defined as $v_d = \tau_p n_g \delta_{i2}$. As expected, the dominant buoyancy force in the larger particles case explains the larger deposition rates in comparison to the smaller particles and also the relatively small difference with respect to the settling rate due to the limited transport contributions attributable to Brownian and thermophoresis forces. In contrast, the much larger actual deposition rate of the small particles case in comparison to its settling value can be explained by the significantly enhanced transport due to thermophoresis and Brownian forces in comparison to that exclusively due to buoyancy.

## 4. Conclusions

Particle deposition in a cubic cavity with opposed thermally active walls have been numerically investigated. Results indicate that a one-way coupling approach with DNS for hydrodynamics and a particle transport model accounting for drag, buoyancy, lift, thermophoresis and Brownian effects is capable of reproducing experimental results in terms of wall deposition velocity. This agreement between numerical and experimental results exists not only for any wall configuration but also for different deposition regimes including thermophoresis-dominated (particle diameter 0.1 μm) and buoyancy-dominated (0.5 μm).

While experimental data was restricted to local values along the cavity bisector of the cavity, numerical results on spatial distribution of deposition rates for each wall allowed to identify preferential particle accumulation spots. It was found that, while thermally active walls exhibit limited inhomogeneities in deposition rates, adiabatic surfaces exhibit high particle concentrations in the vicinity of the corners where hot and cold walls meet. It should be noted that in real physical systems there cannot be a strictly discontinuous gradient where hot and cold meet, but a smooth transition between temperatures. Probably, under these circumstances, the turbulence intensities near these regions, and therefore particle deposition rate, would be more moderate than those predicted by the present DNS.

Current efforts are directed to use this model in more complex geometries characterized by the presence of obstacles that notably interfere with the dominant circulating feature that characterizes the cavity flow used in this work. The expected results might be of interest in using

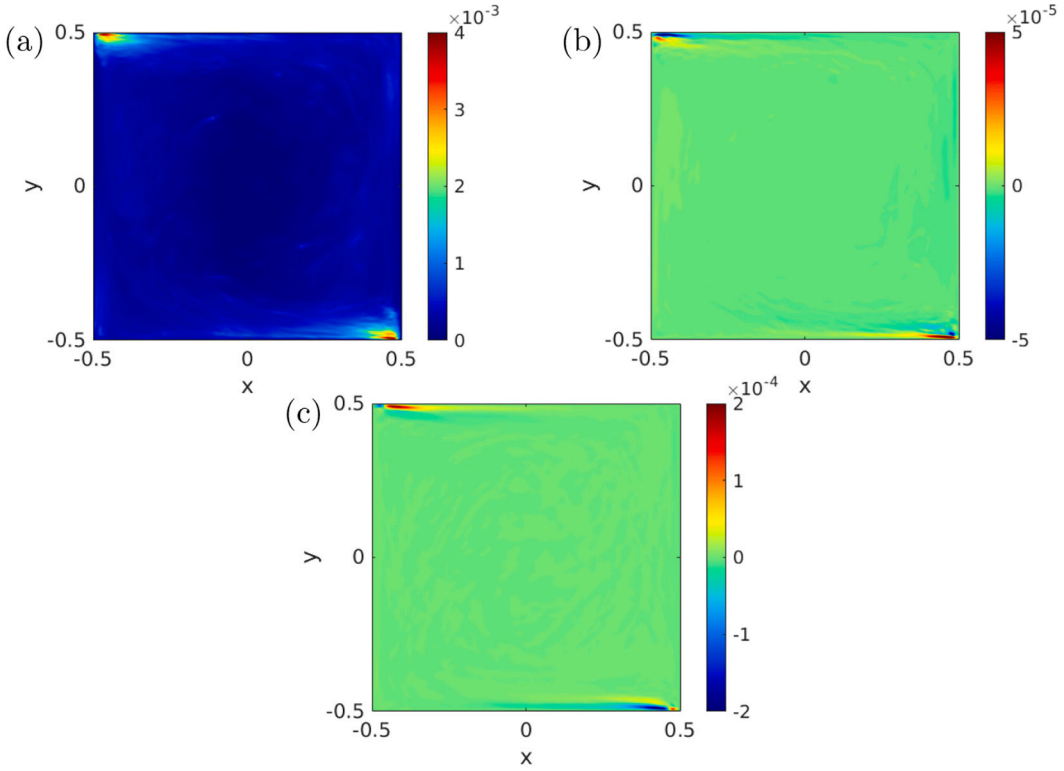


**Fig. 5.** Turbulent fluxes $\langle w'^2 \rangle$ (a), $\langle v'w' \rangle$ (b) and $\langle w'u' \rangle$ (c) near one adiabatic wall at $z = 0.499$.

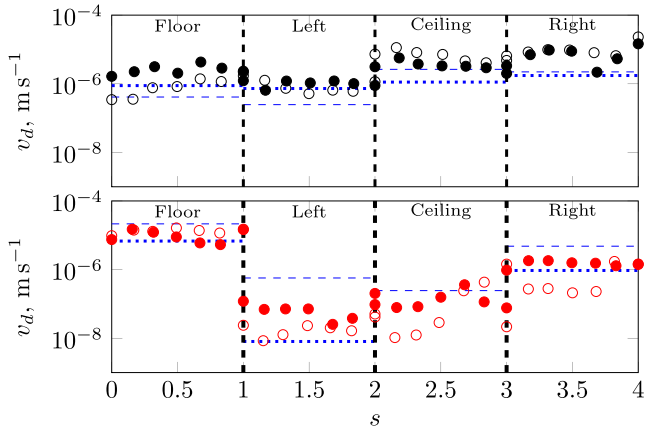


**Fig. 6.** Experimental and numerical comparison of particle deposition velocity for two particle sizes: $d_p = 0.1$ μm (black) and $d_p = 0.5$ μm (red). Symbols correspond to two realizations of the experiments and blue dashed line shows the wall-average numerical value. Dashed horizontal blue lines indicate the wall-average particle deposition velocity from the current DNS. Dotted lines show the values obtained from the boundary layer models in [22]. (For interpretation of the references to colour in this figure legend, the reader is referred to the web version of this article.)

thermal flow control to minimize soiling in valuable surfaces.

## CRediT authorship contribution statement

**Alexandre Fabregat:** Methodology, Software, Validation, Formal analysis, Investigation, Data curation, Writing – original draft, Visualization, Funding acquisition. **Jordi Pallarès:** Conceptualization, Methodology, Validation, Formal analysis, Investigation, Supervision, Writing – review & editing, Project administration, Funding acquisition.

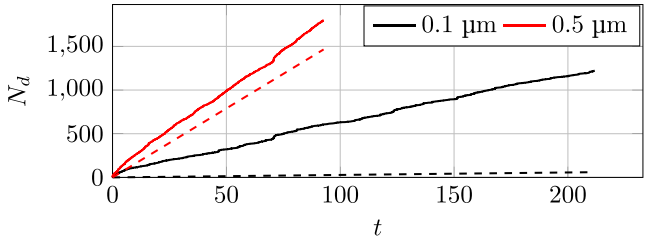


**Fig. 7.** Total deposition rate for two particles sizes: $d_p = 0.1$ μm (black) and $d_p = 0.5$ μm (red). Dashed lines indicate the deposition rate under the settling velocity regime for each diameter size. (For interpretation of the references to colour in this figure legend, the reader is referred to the web version of this article.)

## Declaration of Competing Interest

The authors declare that they have no known competing financial interests or personal relationships that could have appeared to influence the work reported in this paper.

## Acknowledgements

This work has been funded by Spanish Ministerio de Ciencia, Innovación y Universidades through the grants DPI2016-75791-C2-1-P and RTI2018-100907-A-I00 (MCIU/AEI/FEDER, UE) and also by the Generalitat de Catalunya through the grant 2017-SGR-1234. The authors thank the Red Española de Supercomputación (RES) for providing the computational resources used in this study under the projects IM-2019-2-0001 and IM-2020-3-0002.

## References


[1] A.C.K. Lai, W.W. Nazaroff, Modeling indoor particle deposition from turbulent flow onto smooth surfaces, J. Aerosol Sci. 31 (2000) 463–476.
[2] L. Bourouiba, E. Dehandschoewercker, J. Bush, Violent expiratory events: on coughing and sneezing, J. Fluid Mech. 745 (2014) 537–563.
[3] L. Bourouiba, The fluid dynamics of disease transmission, Annu. Rev. Fluid Mech. 53 (2021) 473–508.
[4] S. Sohrabi, J. Zheng, E. Finol, Y. Liu, Numerical simulation of particle transport and deposition in the pulmonary vasculature, J. Biomech. Eng. 136 (2014), 121010.
[5] J. Grau-Bové, M. Strlič, Fine particulate matter in indoor cultural heritage: a literature review, Heritage Sci. 1 (2013) 8.
[6] J. Kalilainen, P. Rantanen, T. Lind, A. Auvinen, A. Dehbi, Experimental investigation of a turbulent particle-laden flow inside a cubical differentially heated cavity, J. Aerosol Sci. 100 (2016) 73–87.
[7] A. Dehbi, J. Kalilainen, T. Lind, A. Auvinen, A large eddy simulation of turbulent particle-laden flow inside a cubical differentially heated cavity, J. Aerosol Sci. 103 (2017) 67–82.
[8] H. Kim, A. Dehbi, J. Kalilainen, Measurements and les computations of a turbulent particle-laden flow inside a cubical differentially heated cavity, Atmos. Environ. 186 (2018) 216–228.
[9] C. Bosshard, A. Dehbi, M. Deville, E. Leriche, A. Soldati, Large eddy simulation of particulate flow inside a differentially heated cavity, Nucl. Eng. Des. 267 (2014) 154–163.
[10] B. Gereltbyamba, C. Lee, Behavior of settling inertial particles in a differentially heated cubic cavity at moderate rayleigh number, J. Mech. Sci. Technol. 32 (2018) 3169–3182.
[11] A. Kirkpatrick, M. Bohn, An experimental investigation of mixed cavity natural convection in the high Rayleigh number regime, Int. J. Heat Mass Transf. 29 (1986) 69–82.
[12] F. Arpino, N. Massarotti, A. Mauro, High Rayleigh number laminar-free convection in cavities: new benchmark solutions, Num. Heat Transf. sB: Fundamentals 58 (2010) 73–97.
[13] C. Cianfrini, M. Corcione, P.P. Dell'Omo, Natural convection in tilted square cavities with differentially heated opposite walls, Int. J. Therm. Sci. 44 (2005) 441–451.
[14] M. Corcione, Effects of the thermal boundary conditions at the sidewalls upon natural convection in rectangular enclosures heated from below and cooled from above, Int. J. Therm. Sci. 42 (2003) 199–208.
[15] D. Das, M. Roy, T. Basak, Studies on natural convection within enclosures of various (non-square) shapes – a review, Int. J. Heat Mass Transf. 106 (2017) 356–406.
[16] K. Hanjalić, S. Vasić, Computation of turbulent natural convection in rectangular enclosures with an algebraic flux model, Int. J. Heat Mass Transf. 36 (1993) 3603–3624.
[17] I. Miroshnichenko, M. Sheremet, Turbulent natural convection heat transfer in rectangular enclosures using experimental and numerical approaches: a review, Renew. Sust. Energ. Rev. 82 (2018) 40–59.
[18] S.S. Ostrach, C. Raghavan, Effect of stabilizing thermal gradients on natural convection in rectangular enclosures, ASME. J. Heat Transf. 101 (1979) 238–243.
[19] G.S. Shiralkar, C.L. Tien, A numerical study of the effect of a vertical temperature difference imposed on a horizontal enclosure, Num. Heat Transf. 5 (1982) 185–197.
[20] T.L. Thatcher, W.A. Fairchild, W.W. Nazaroff, Particle deposition from natural convection enclosure flow onto smooth surfaces, Aerosol Sci. Technol. 25 (1996) 359–374.
[21] A. Fabregat, J. Pallares, Heat transfer and boundary layer analyses of laminar and turbulent natural convection in a cubical cavity with differently heated opposed walls, Int. J. Heat Mass Transf. 151 (2020), 119409.
[22] J. Pallares, A. Fabregat, Prediction of particle deposition on the walls of a cubical cavity with differentially heated opposed walls using heat and mass transfer laminar mixed convection boundary layer models, Int. J. Heat Mass Transf. 165 (2021), 120691.
[23] M. Elimelech, X. Jia, J. Gregory, R. Williams, Particle Deposition and Aggregation: Measurement, Modelling and Simulation, Colloid and Surface Engineering Series, Elsevier Science, 1998.
[24] P.F. Fischer, J.W. Lottes, S.G. Kerkemeier, Nek5000 Web page. Http://nek5000.mcs.anl.gov, 2008.
[25] J.D. Scheel, M.S. Emran, J. Schumacher, Resolving the fine-scale structure in turbulent Rayleigh–Bénard convection, New J. Phys. 15 (2013), 113063.
[26] P.W. Longest, S. Vinchurkar, Effects of mesh style and grid convergence on particle deposition in bifurcating airway models with comparisons to experimental data, Med. Eng. Phys. 29 (2007) 350–366.
[27] V. Michalis, A. Kalarakis, E. Skouras, V. Burganos, Rarefaction effects on gas viscosity in the Knudsen transition regime, Microfluid. Nanofluid. 9 (2010) 847–853.
[28] C. Crowe, J. Schwarzkopf, M. Sommerfeld, Y. Tsuji, Multiphase Flows with Droplets and Particles, 2nd ed., CRC Press, 2011.
[29] M.D. Allen, O.G. Raabe, Slip correction measurements of spherical solid aerosol particles in an improved millikan apparatus, Aerosol Sci. Technol. 4 (1985) 269–286.
[30] L. Talbot, R.K. Cheng, R.W. Schefer, D.R. Willis, Thermophoresis of particles in a heated boundary layer, J. Fluid Mech. 101 (1980) 737–758.
[31] J. Mclaughlin, Inertial migration of a small sphere in linear shear flows, J. Fluid Mech. 224 (1991) 261–274.
[32] H. Ounis, G. Ahmadi, J.B. McLaughlin, Brownian particle deposition in a directly simulated turbulent channel flow, physics of fluids a, Fluid Dynam. 5 (1993) 1427–1432.
[33] I.E. Barton, Exponential-Lagrangian tracking schemes applied to stokes law, J. Fluids Eng. 118 (1996) 85–89.